

Effect of Blade Profiles on the performance of Bidirectional Wave Energy Turbine

P. Madhan Kumar¹, Abdus Samad^{1,}*

¹ Wave Energy and Fluids Engineering Laboratory, Department of Ocean Engineering, Indian Institute of Technology Madras, Chennai 600036, India

Abstract. To fulfill the ever growing demands of world energy consumption, the wave energy should be extracted economically. The oscillating water column is most commonly used to extract energy from waves. It consists of a chamber in which waves drives the entrapped air column to rotate the Wells turbine. The Wells turbine is a self-rectifying low-pressure axial reaction turbine with 90° stagger angle. These turbines consist of symmetrical airfoil profile to achieve unidirectional rotation for the bi-directional airflow. The turbine performance predominantly depends on the aerodynamic characteristics of the airfoil profile used. In this study, the performance of Wells turbine with various symmetrical airfoil profiles was analysed using ANSYS CFX 14.5. The CFD analysis was performed by solving three dimensional steady Reynolds averaged Navier-Stokes equation with k- ω SST turbulence closure model. The reference geometry has NACA0015 as blade profile and the CFD results were compared with the experimental values. The performance characteristics of the new airfoil profiles were compared with the reference case to analyse the suitability of airfoils in wave energy extraction. The NACA0021 airfoil profile showed better performance in the post-stall regime compared to the NACA0015 and the S1046 airfoil profiles.

Keywords: Wave energy, Wells turbine, Airfoil profiles, CFD

1 Introduction

The Wells turbine is used to extract the energy from the bidirectional airflow inside the oscillating water column (OWC). It consists of a symmetrical airfoil with 90° stagger angle. It provides unidirectional torque for the oscillating flow without any guide vanes, which makes the power take-off system simple [1]. On the contrary, the Wells turbine has limitations such as narrow operating range, noisy operation, and poor starting characteristics. The performance of the turbomachines primarily depends on the airfoil profile used. There were many studies done on the effect of different symmetrical and non-symmetrical airfoil profiles on the performance of Wells turbine. The airfoils with thicker profiles improve starting characteristics and performance of the Wells turbine [2,3]. The stall characteristics of Wells turbine can be improved by optimization of airfoil profile. Webster et al. [4] optimized the NACA0015 airfoil profile and reported better stall characteristics. Setoguchi et al. [5] investigated the performance characteristics of four different airfoil profiles and concluded that NACA four-digit airfoil profiles with 20% thickness ratio are suitable for better performance of Wells turbine. Takao et al. [6] compared the performance characteristics of airfoils with sweep. They studied the following airfoil profiles NACA0015,

NACA0020, CA9, and HSI 15-262123-1576 and reported that NACA0015 is the desirable airfoil profile to achieve better performance. The airfoil profile CA9 with solidity 0.64 is suitable to achieve better performance in the real sea conditions [7]. Takao et al. [8] investigated airfoil profiles NACA0015, NACA0020 and modified Eppler472 and reported that modified Eppler472 airfoil profile is superior to the other profiles analysed. Mohamed et al. [9] proposed the use of non-symmetrical airfoil profiles in the Wells turbine. The optimization of airfoil profile in Wells turbine is also investigated by many researchers [9-11]. From the above studies, it is evident that the performance of Wells turbine is highly influenced by the nature of airfoil profile used. To analyse the influence of airfoil profiles on the Wells turbine performance three airfoil profiles are used in this study. Based on the previous studies airfoils NACA0015 and NACA0021 are chosen as the suitable candidates for the blade profile. Mohamed [12] evaluated the effects of various symmetrical and non-symmetrical airfoil profiles on the performance of Darrieus turbine. He reported that S1046 airfoil profile shown better aerodynamic characteristics and improved efficiency compared to other profiles. Hence S1046 airfoil profile is also included in this numerical study. It is symmetrical in nature and suitable for Wells turbine application. The performance characteristics of the

* Corresponding author: samad@iitm.ac.in

airfoil profiles are numerically analysed and compared with the reference case. The fluid dynamics is also explained in detail with the help of post-processed figures.

2 Description of rotor geometry

The Wells turbine geometry used in the work of Torresi et al. [13] is taken as the reference case for this study. It consists of NACA0015 as the blade profile. The specifications of the reference geometry are provided in Table 1.

Table 1. Reference geometry specifications

Blade profile	NACA0015
Number of blades	8
Chord length	125 mm
Tip diameter	600 mm
Hub diameter	400 mm
Mean radius	250 mm
Solidity	0.64
Tip clearance	1.25 mm (1% Chord length)
Rotational speed	2000 rpm

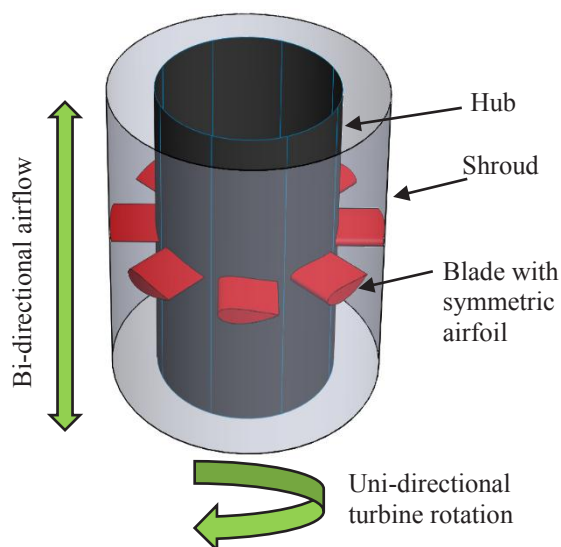


Fig. 1. Schematic of Wells turbine

The schematic of Wells turbine is illustrated in Figure 1. The modified geometries are created by replacing the NACA0015 airfoil profile with other airfoil profiles and all other design parameters are preserved same as the reference turbine. The description of the airfoil profiles used in this study is provided in Table 2 and the comparison of airfoil profiles used is shown in Fig 2.

Table 2. Details of airfoil profiles

Blade profile	Maximum thickness (%C)	Maximum thickness location (%C)
NACA0015	15	30

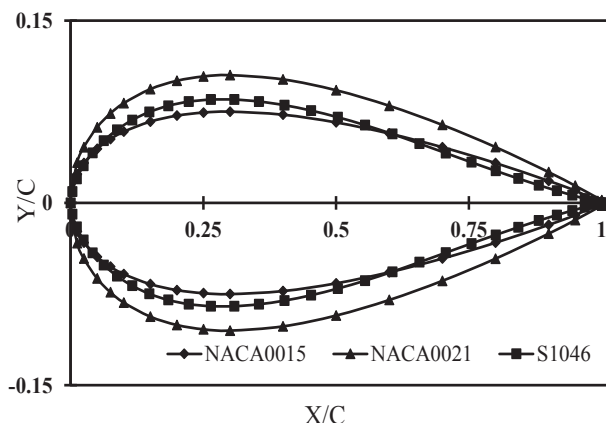


Fig. 2. Comparison of airfoil profiles

NACA0021	21	30
S1046	17	30.8

3 Numerical formulation

The computational domain for numerical analyses is shown in Fig 3. To minimize the computational time, a single blade with rotational periodicity is chosen as the computational domain. The upstream and the downstream length is fixed as 4C and 6C respectively. The computational domain was discretized with unstructured tetrahedral elements using ICEM CFD. To capture the near wall flow physics, 20 layers of prism elements were generated around the blades with a stretching ratio of 1.2.

The surface mesh of the computational domain is presented in Fig 4. The numerical analyses were done by solving incompressible steady three dimensional Reynolds averaged Navier-Stokes (RANS) equation using coupled solver ANSYS CFX 14.5. It solves the aerodynamic equations for (u, v, w, p) as a single system [14]. The rotation of turbine is realized by implementing the rotating reference method. The boundary conditions are applied in CFX-Pre. Air at 25°C is taken as the working fluid and the compressibility effects are neglected. Uniform velocity and zero pressure gradient boundary conditions are given on the inlet and outlet respectively. The blade and hub are imposed with no-slip boundary condition whereas the shroud is kept as counter-rotating no-slip wall. The lateral faces of the computational domain is taken as periodic faces to account for the rotational periodicity. The turbulence intensity at the inlet is fixed as 5% (medium intensity) and $k-\omega$ SST with automatic wall function is chosen as the turbulence closure model. It is suitable for flows with severe adverse pressure gradient and separation [15]. It activates $k-\epsilon$ model away from the wall and $k-\omega$ model closer to the wall, thereby incorporating the merits of both turbulence models. A high-resolution advection scheme is employed for spatial discretization to ensure second-order accuracy. The numerical simulations are run up to 2000 iterations and the residual convergence criteria value is set to $1e-5$ to ensure convergence.

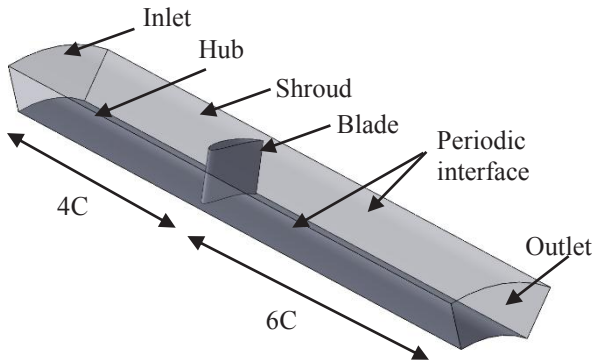


Fig. 3. Schematic of Wells turbine

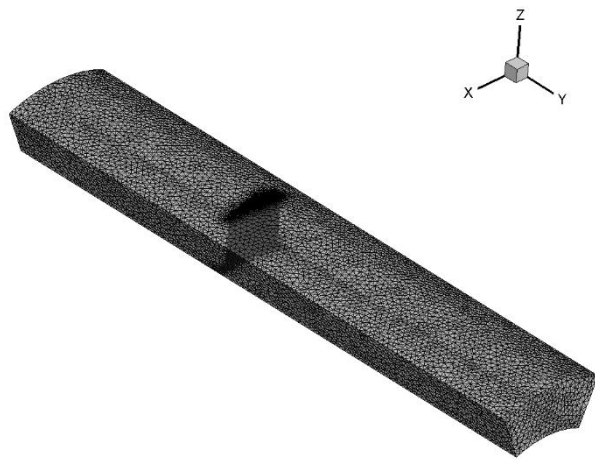


Fig. 4. Surface mesh of the computational domain

The performance characteristics of the Wells turbine is analysed by the following non-dimensional parameters.

Torque coefficient

$$T^* = \frac{T}{\rho \omega^3 R_{tip}^5}$$

1

Stagnation pressure drop coefficient

$$\Delta p^* = \frac{\Delta p_o}{\rho \omega^2 R_{tip}^2}$$

2

Efficiency

$$\eta = \frac{T \omega}{Q \Delta p_o}$$

3

Flow coefficient

$$U^* = \frac{U_\infty}{U_{tip}}$$

4

Where T is the torque, ρ is the density of air, ω is the angular velocity of the turbine, R_{tip} is the tip radius, Δp_o is the stagnation pressure drop, Q is the discharge, U_∞ is the free stream inlet velocity and U_{tip} is the blade tip

velocity. The performance characteristics of the Wells turbine is obtained by plotting the above non-dimensional parameters against the flow coefficient (FC) U^* .

4 Results and discussion

4.1 Grid independence study

The grid independence study is performed to select the mesh with optimum resolution. It is essential to perform this study as the computational time will increase with an increase in a number of grid elements. To perform this study meshes with three resolutions such as coarse, medium and fine is selected and the efficiency is compared for the entire flow range. The results of all

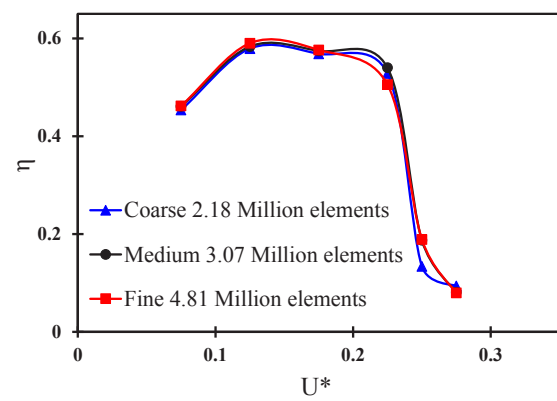


Fig. 5. Grid independence study

grids are almost same and the maximum deviation between the medium and fine grid is 6.8% which is acceptable. Hence the medium grid with 3 million elements is retained for numerical simulations throughout this study. The plot of grid independency study is shown in Fig 5.

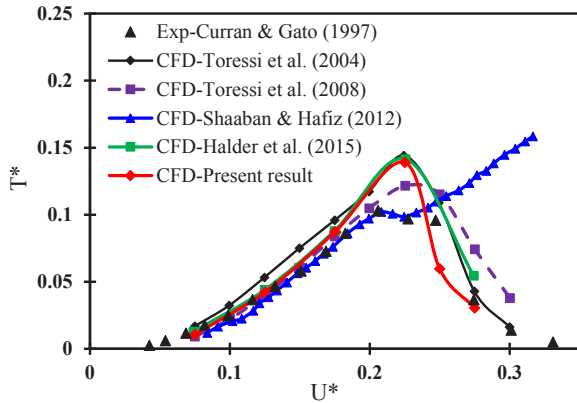
4.2 CFD Validation

To ensure the numerical accuracy of the simulations performed the present numerical results are validated with the experimental results of Curran and Gato [16] and the numerical results of [13,17,18,19]. The CFD validation of the numerical results is presented in Fig 6. The performance characteristics of the Wells turbine for the entire flow range is plotted and verified. From the figure, it is evident the present numerical results follow the same trend as the existing CFD results except for the work of Shaaban and Abdel Hafiz [18]. In their work, they reported that the steady RANS model failed to predict the stall phenomenon of the Wells turbine.

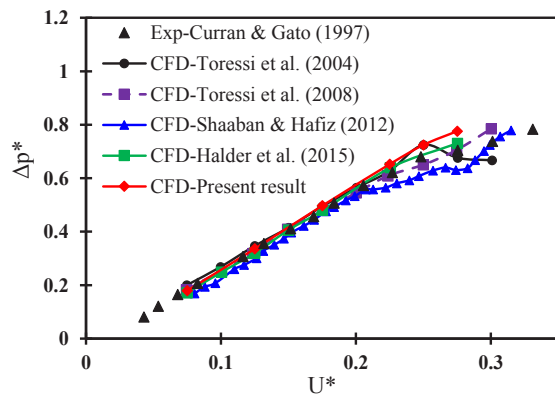
4.3 Effect of Airfoil Profiles

The present work investigates the effect of three different airfoil profiles on the performance of Wells turbine. The study has been done for the entire flow

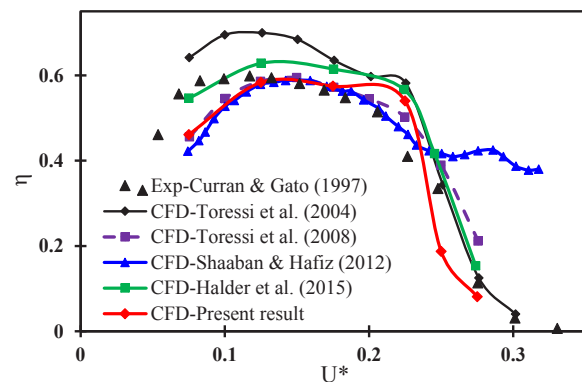
range, including the post-stall regime. The comparison of the performance characteristics of the Wells turbine for different airfoil profiles is illustrated in Fig 7. It can be observed that all three airfoil profiles undergo stall after $U^*=0.225$, which is denoted by a rapid decrease in torque and efficiency due to flow separation.



a) Torque coefficient

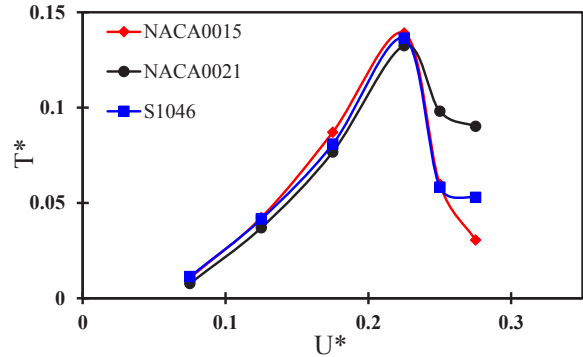


b) Pressure coefficient

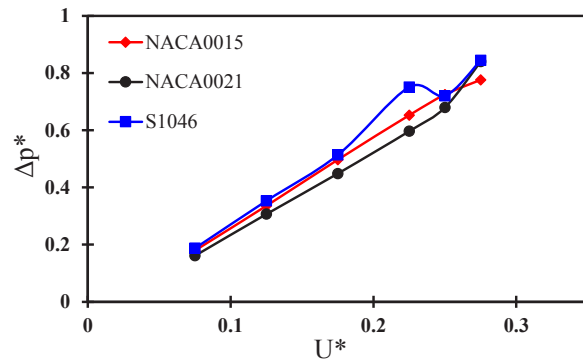


c) Efficiency

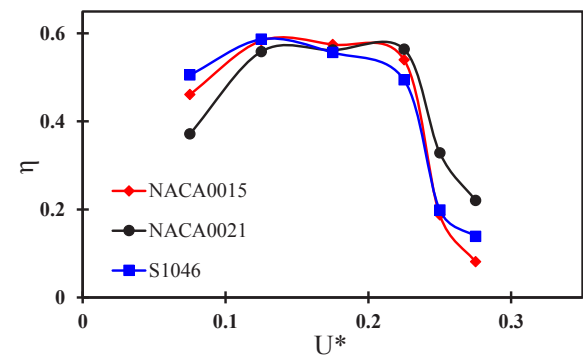
Fig. 6. Validation of numerical results



a) Torque coefficient



b) Pressure coefficient



c) Efficiency

Fig. 7. Comparison of various airfoil profiles

From Fig. 7a, it is evident that the maximum torque coefficient is obtained for NACA0015 profile followed by S1046 and NACA0021. The NACA0021 airfoil profile performs better in the post-stall regime and the drop in torque and efficiency is not severe as compared to the other airfoil profiles. The pressure drop of the NACA0021 airfoil profiles is lower than the NACA0015 and S1046 airfoil profiles (Fig. 7b). The peak efficiency is obtained for the S1046 airfoil profile at $U^*=0.125$, however, the difference between the maximum efficiency of S1046 and NACA0015 is not significant. At low FC ($U^*=0.075$), it can be noticed that the efficiency of S1046 is significantly higher than the other airfoil profiles. The efficiency of NACA0021 is better in the post-stall regime compared to the S1046 and NACA0015 airfoil profiles. The static pressure distribution on the blade suction surface of the different airfoil profiles is presented in Fig 8.

At $U^*=0.075$, the pressure distribution is almost same for all the airfoil profiles. With the increase in FC, the incidence is also increased. At $U^*=0.225$, the suction pressure is minimum at the leading edge (LE) for all the cases. This pressure difference between the suction and the pressure side creates the lift force. At FC $U^*=0.225$, the peak torque is obtained for all the cases (Fig 7a). At $U^*=0.275$, a large low-pressure region is noticed on the suction side (SS) of the blade. This can be attributed to the high incidence of the flow at high FCs. The low-pressure region on the blade SS implicates adverse pressure gradient and it leads to flow separation. This can be corroborated by a sudden drop in torque and efficiency in Fig 7a and 7c. In order to analyse the stall phenomenon in detail, the surface streamlines on the blade suction surface are presented in Fig 9.

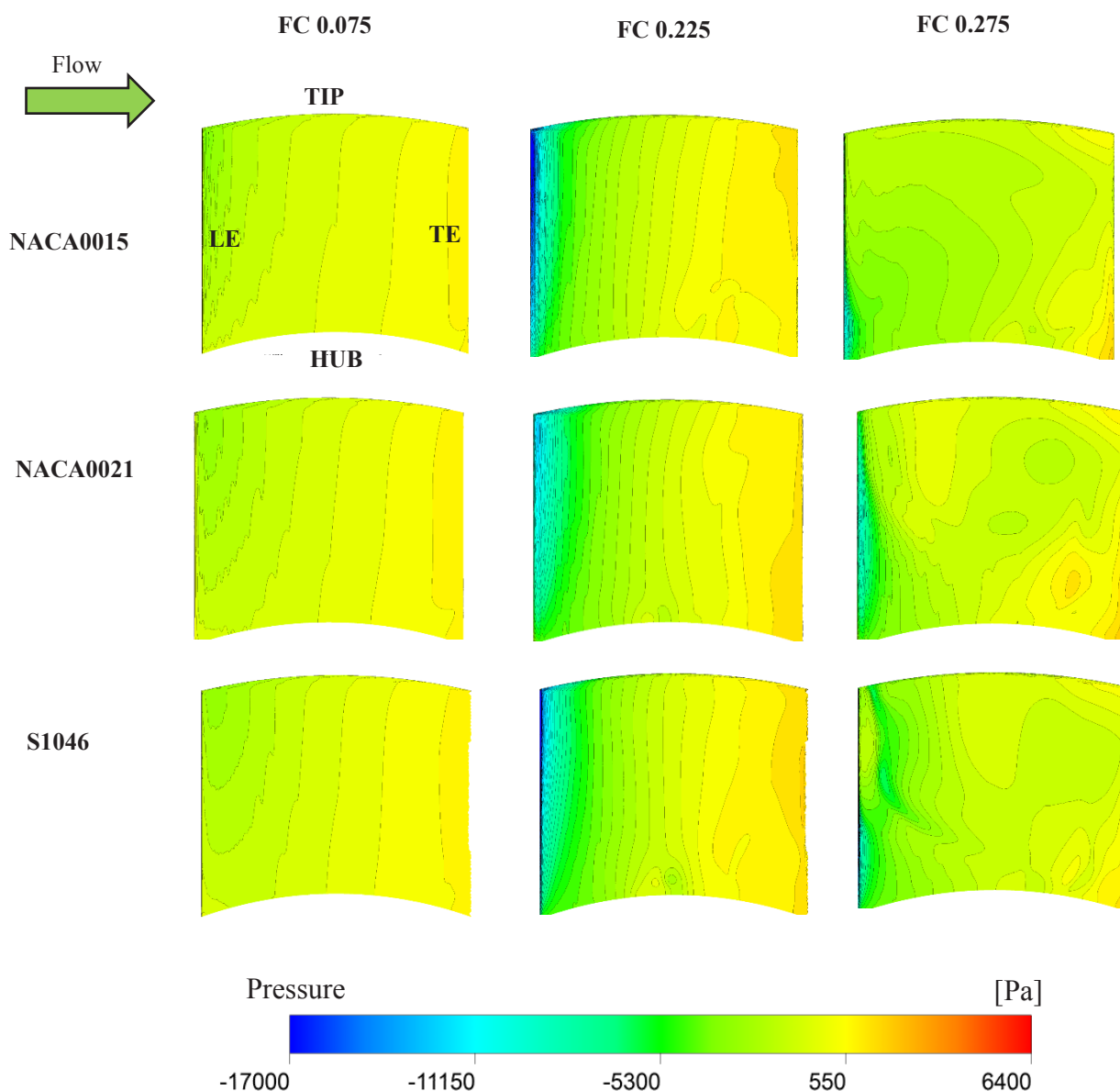


Fig. 8. Static pressure distribution on the blade suction surface

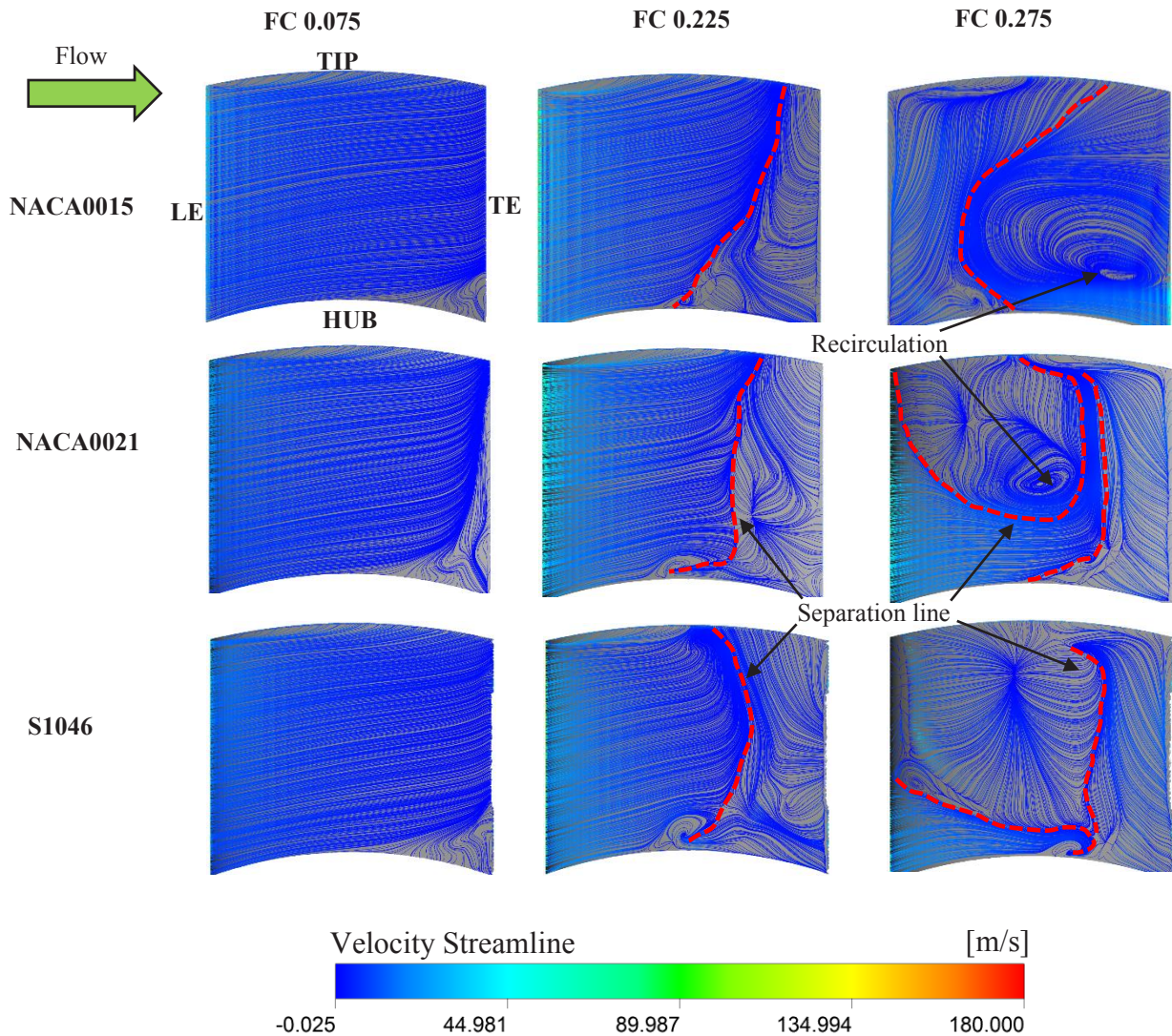


Fig. 9. Surface streamlines on the blade suction surface

At low FC ($U^*=0.075$), the flow is completely attached for all the cases. However, the hub separation is observed in all the three airfoil profiles. Albeit the flow is attached the torque produced is less because of the low incidence. At FC $U^*=0.225$, the peak torque is obtained for all the airfoil profiles and the flow separation region is shown in Fig 9. The area between the separation line and the trailing edge implicates the separated region of flow. In this case, it is evident that flow separation is confined closer to the trailing edge of the blade. With the increase in FCs, the separation line advances towards the leading edge and gradually stall occurs. It can be seen from Fig 9 at high FC ($U^*=0.275$), the separation line is further advanced towards the leading edge of the blade and the complete flow separation takes place for all the cases. It explains the sudden drop in torque and efficiency in the Fig 7a and 7c. At high FC, the effect of tip leakage flow is severe and it aids in the inception of stall phenomenon. The NACA0021 airfoil seems to have better performance in the post-stall regime compared to NACA0015 and S1046

airfoil profiles. The flow separation region of NACA0021 is relatively smaller than the other cases and it corroborates the higher torque and efficiency of NACA0021 in the post-stall regime from Fig 7a and 7c. In Fig 10, the streamlines on the blade midspan are presented. It can be witnessed from the figure that the flow is fully attached at low FC ($U^*=0.075$). As explained earlier, due to low incidence the flow is completely attached for all the airfoil profiles. At FC $U^*=0.225$, a recirculation zone is visible at the SS of the trailing edge for all cases of airfoil profiles. Since the flow separation is limited to the trailing edge region and due to high incidence, the peak torque is achieved at this FC. With further increase in FC ($U^*=0.275$), the separation line advances towards the SS of the leading edge and the stall occurs. The separated region of the NACA0015 airfoil profile is larger compared to NACA0021 and S1046 airfoil profiles. This can be attributed to the poor performance of NACA0015 in the post-stall regime. Moreover, the performance of NACA0021 airfoil is relatively better than the other airfoil profiles.

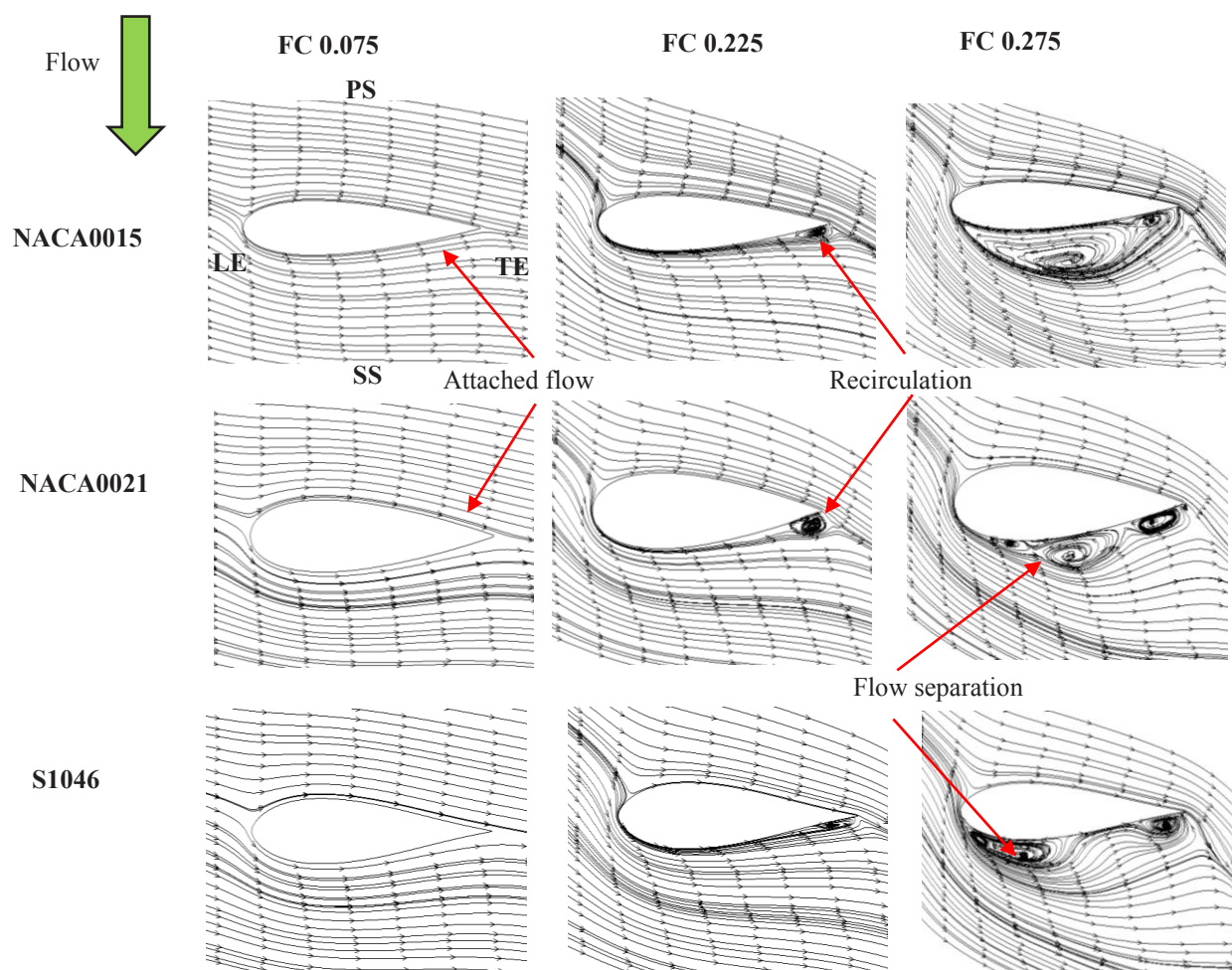


Fig. 10. Streamlines on the blade midspan

5 Conclusion

In this numerical study, the performance of Wells turbine with different airfoil profiles was investigated. Three symmetrical airfoil profiles such as NACA0015, NACA0021 and S1046 was selected for this study. The prominent conclusions drawn from this study were listed below.

- The performance of Wells turbine predominantly depends on the airfoil profile used.
- The maximum peak efficiency was achieved in the case of S1046 airfoil whereas the maximum peak torque was obtained in case of the NACA0015 airfoil.
- The NACA0021 airfoil showed better performance in the post-stall regime.
- Furthermore, optimization of these airfoil profiles is recommended to obtain an optimized airfoil profile with improved performance characteristics.

6 References

1. Raghunathan, S., C. P. Tan, and N. A. J. Wells. *Journal of Energy* **6**, 157-160. (1982)
2. Raghunathan, S., and C. P. Tan. *International journal of heat and fluid flow* **6**, no. 1, 17-22. (1985)
3. Raghunathan, S. *Progress in Aerospace Sciences* **31**, no. 4, 335-386. (1995)
4. Webster, M., and L. M. C. Gato. In *The Ninth International Offshore and Polar Engineering Conference*. International Society of Offshore and Polar Engineers, (1999).
5. Setoguchi, T., T. W. Kim, M. Takao, A. Thakker, and S. Raghunathan. *International journal of ambient energy* **25**, no. 3, 137-150. (2004)
6. Takao, Manabu, Ajit Thakker, Rahil Abdulhadi, and Toshiaki Setoguchi. *International Journal of Sustainable Energy* **25**, no. 01, 53-61. (2006)

7. Thakker, A., and R. Abdulhadi. *International Journal of Rotating Machinery*, (2007).
8. Takao, Manabu, Toshiaki Setoguchi, Shuichi Nagata, and Kazutaka Toyota. *OMAE Proceedings*, 625-632. (2008)
9. Mohamed, M. H., G. Janiga, and D. Thévenin. In *ASME Turbo Expo Conference, (GT2008-50815), Berlin, Germany*. (2008).
10. Mohamed, M. H., G. Janiga, E. Pap, and D. Thévenin. *Energy* **36**, no. 1, 438-446. (2011)
11. Gato, L. M. C., and J. C. C. Henriques. *ASME-PUBLICATIONS-FED*, **238**, 623-630. (1996)
12. Mohamed, M. H. *Energy* **47**, no. 1, 522-530. (2012)
13. Torresi, M., S. M. Camporeale, P. D. Strippoli, and G. Pascazio. *Renewable Energy* **33**, no. 4 (2008): 735-747.
14. CFX, ANSYS. "Solver Theory Guide. Ansys." *Inc., Canonsburg, PA*. (2011)
15. Menter, Florian R. *AIAA journal* **32**, no. 8, 1598-1605. (1994)
16. Curran, R., and L. M. C. Gato. *Proceedings of the Institution of Mechanical Engineers, Part A: Journal of Power and Energy* **211**, no. 2, 133-145. (1997)
17. Torresi, M., S. M. Camporeale, G. Pascazio, and B. Fortunato. In *59 Congresso ATI, Genova, Italy*. (2004)
18. Shaaban, S., and A. Abdel Hafiz. *Energy Conversion and Management* **61**, 51-58. (2012)
19. Halder, Paresh, Abdus Samad, Jin-Hyuk Kim, and Young-Seok Choi. *Energy* **86**, 219-231. (2015)